Intertwined spin and phonon correlations across the magnetic compensation temperature in magnetoelectric $Li_{0.5}Fe_{2.5-x}Cr_xO_4$

P. Srikanth Patnaik,[1] Amit Kumar,[2,3] Anushree Roy,[1,*] and S. M. Yusuf[2,3,†]
[1]*Department of Physics, Indian Institute of Technology Kharagpur, Kharagpur 721302, India*
[2]*Solid State Physics Division, Bhabha Atomic Research Centre, Mumbai 400085, India*
[3]*Homi Bhabha National Institute, Anushaktinagar, Mumbai 400094, India*

(Received 17 April 2023; revised 7 July 2023; accepted 14 July 2023; published 31 July 2023)

Recent reports in the literature suggest that emerging magnetic phenomena, like magnetic compensation, magnetic reorientation, etc., in correlated complex oxide systems arise due to the coupling of electronic spin with phonons in the lattice. Here, we investigate the interlinkage of electronic spin with phonon dynamics across tetrahedral and octahedral magnetic sublattices in $Li_{0.5}Fe_{2.5-x}Cr_xO_4$ ($x = 1.1$, 1.3, 1.5, and 1.6) that shows magnetic compensation. Temperature-dependent micro-Raman spectroscopic measurements exhibit the anomalies in phonon wave number vs temperature plots below the magnetic-ordering temperature. The estimated spin-phonon coupling strengths in all compounds over the entire temperature range of interest reveal a dual nature of magnetoelastic coupling at both sublattice sites in this system. The coupling strength for the tetrahedral sublattice site is found to be an order of magnitude higher in the regime between near-compensation and phase-transition temperatures than over the low-temperature regime, while the same nearly vanishes above the compensation temperature for the octahedral site. The study suggests the possible role of phonon in establishing the magnetic compensation phenomenon involving two magnetic sublattices. Additionally, the Fano line shape of the A_{1g} mode in the tetrahedral site, especially the variation of the Fano asymmetry parameter with temperature, carries the signature of a cross talk between spin and lattice degrees of freedom in this system. The anomaly in the variation of Raman spectral width of the same mode with temperature suggests a relatively strong electron-phonon coupling in these compounds. The study demonstrates a complex interplay between electronic spin dynamics, electrical and lattice degrees of freedom in two magnetic sublattices of $Li_{0.5}Fe_{2.5-x}Cr_xO_4$.

DOI: 10.1103/PhysRevB.108.014438

I. INTRODUCTION

In complex oxide systems, exhibiting magnetic compensation via spin reorientation [1–7], multiferrocity [8–12], solitonic lattice [13], or domain-wall inversion [14,15], a crucial role is played by the lattice degrees of freedom in steering their magnetic behavior. In the presence of multiple magnetic sublattices, the coupling of phonon and electronic spin becomes complex. For example, cross talk between two magnetic sublattices having Sm^{3+} and Fe^{3+} in $SmFeO_3$ through extraordinarily strong nonlinear spin-phonon interaction of multiple orders has been demonstrated [16]. It has been shown that the intrinsic ordering of spin of Sm^{3+} in the exchange field of Fe^{3+} at the other magnetic sublattice site could be activated only by coupling of spin and lattice degrees of freedom. An incommensurate novel magnetic state in the orthoferrite $TbFeO_3$ exhibits an anomalously large number of higher-order harmonics, which arises due to the interaction of Tb domain walls with Fe magnetic sublattice via Yukawa-type interactions by exchanging spin waves [17]. Such nonlinear material responses determine microscopic mechanisms behind the coupling of spins at different lattice sites to yield exotic magnetic phases and their potential applications in technology.

In addition to the coupling of phonons with spin degrees of freedom, the interaction of phonons with the electronic density of states, often referred to as electron-phonon coupling [18–22], has been used to explain many fascinating properties of various correlated systems. Few recent reports have demonstrated the existence of both electron-phonon and spin-phonon coupling in complex oxides. In two-dimensional epitaxial thin film of Fe_3O_4, the magnetic spin reorientation and Verwey transition below a certain temperature have been explained in light of the correlation between these coupling schemes and charge-orbital ordering in the system [23]. Both coupling schemes are also exploited to explain metal-insulator phase transition and paramagnetic–to–all-in/all-out spin ordering in pyrochlore irridate $(Eu_{1-x}Bi_x)_2Ir_2O_7$ [24]. It is to be noted that the coexistence of spin-phonon and electron-phonon coupling in such materials opens a new horizon beyond spin electronics, due to the availability of phonon, in addition to spin and charge of electrons, as a third degree of freedom with implications in technological applications.

Here, we have demonstrated the simultaneous existence of spin-phonon and electron-phonon coupling in $Li_{0.5}Fe_{2.5-x}Cr_xO_4$ ($x = 1.1$, 1.3, 1.5, and 1.6). It is a ferrimagnetic lithium-based spinel dielectric material with high ionic and electronic conductivities [25]. Recent studies suggest that

*anushree@phy.iitkgp.ac.in
†smyusuf@barc.gov.in

TABLE I. Values of T_{comp}, T_m, and T_c for $Li_{0.5}Fe_{2.5-x}Cr_xO_4$ with $x = 1.1$, 1.3, 1.5, and 1.6 (from Ref. [25]).

Composition (x)	T_{comp} (K)	T_m (K)	T_c (K)
1.1	437	540	608
1.3	305	430	540
1.5	256	350	417
1.6	280	390	463

the richness in the magnetoelectric properties in these compounds is strongly governed by the interlinkage between the electric and magnetic degrees of freedom [25,26]. The presence of two magnetic ions, Fe^{3+} and Cr^{3+}, at two magnetic sublattices (octahedral and tetrahedral) makes the interactions particularly complex. Below the magnetic-ordering temperature T_c the polarity of the net magnetic moment changes, with a maximum (at T_m) and zero moments (at T_{comp}) in between. Molecular-field theory suggests that superexchange interaction between intrasublattice interactions in these compounds is weaker than intersublattice interactions via oxygen atoms. There exists a cross talk between two sublattices via strong negative exchange interaction. The reported values of T_{comp}, T_m, and T_c for different compositions of $Li_{0.5}Fe_{2.5-x}Cr_xO_4$ ($x = 1.1$, 1.3, 1.5, and 1.6) are available in Table I. The systematic drop in the value of T_{comp}, T_m, and T_c ions up to $x = 1.5$ has been attributed to an average spin dilution and the increase in the substitutional disorder with the increase in the doping concentration of Cr^{3+}. There is a slight increase in T_{comp}, T_m, and T_c for $x = 1.6$, which may be due to the change in the crystal structure of $Li_{0.5}Fe_{0.9}Cr_{1.6}O_4$ [25].

Both sublattices are also involved in determining the electrical conductivity of the compound. While the Li^+ ions in both crystallographic sites determine ionic conduction, electron transport is governed by a small polaron hopping mechanism between both sublattice sites. Interestingly, the changes in the slope of both ionic and electronic conductivity vs temperature plots at T_c and T_{comp} suggest a strong coupling of magnetic and electrical degrees of freedom in these compounds. The evolution of frequency exponent (n) of ac conductivity with temperature, which explains the microscopic mechanism for the translational motion of the ions also shows a change in trend at T_c and T_{comp}.

In this paper, we address the following: Does the phonon dynamics $Li_{0.5}Fe_{2.5-x}Cr_xO_4$ play any role in determining the magnetic compensation phenomenon? Using temperature-dependent micro-Raman spectroscopy over a wide temperature range, spin-phonon coupling strengths for both octahedral and tetrahedral magnetic sublattice sites are estimated. A dual nature of magnetoelastic coupling at both sublattice sites is observed. It is demonstrated that with the increase in temperature, the magnetoelastic coupling at the tetrahedral sublattice site enters from a regime of low coupling strength to a regime with an order of magnitude higher coupling strength just below the T_{comp} and remains there till T_c. However, over this high-temperature range, the coupling strength is negligible for the octahedral sublattice site. These observations, along with the noted one-to-one correlation between magnetization and shift of phonon wave number due to coupling, further suggest the participation of phonon in coupling two magnetic lattice sites. The prominent A_{1g} mode in the tetrahedral site also could be best fitted with the Fano line shape, further confirming that the Fe^{3+} ions present in the tetrahedral site play an important role in electron-lattice coupling. The electron-phonon interaction strength, determined by the Fano asymmetric parameter $1/|q|$, decreases with an increase in temperature. The anomalous behavior of this parameter between T_{comp} and T_c having a maximum in between confirms phonon-mediated magnetic exchange interaction between two sublattices. Furthermore, the variation of phonon linewidth with the temperature of the same A_{1g} mode mentioned above exhibits strong electron-phonon coupling in these compounds. A strikingly similar trend of the variation of the contribution of the electronic states in Raman linewidth and n (frequency exponent of ac conductivity) with temperature, along with changes in the slope of the plots at T_{comp} and T_c, strongly suggests a significant role of the phonon in the coupling of magnetization dynamics and electrical transport mechanism in these compounds.

II. EXPERIMENTAL DETAILS

$Li_{0.5}Fe_{2.5-x}Cr_xO_4$ (for $x = 1.1$, 1.3, 1.5, and 1.6) were prepared by the standard double-sintering ceramic technique. Fe_2O_3, Cr_2O_3, and Li_2CO_3 were mixed in different stoichiometric ratios to vary x. The details of the synthesis procedure are available in Ref. [26]. Micro-Raman spectroscopic measurements of these compounds were carried out by using a single-monochromator (Labram Evolution, Horiba France) Raman spectrometer. The spectrometer is equipped with a confocal microscope (BX41, Olympus, Japan) as the incident-collection optics and a Peltier-cooled charge-coupled device (Syncerity, Horiba France) as the detector. All spectra were recorded in backscattering geometry using a 50 × L objective lens of the microscope. A diode laser (LAS-532-100-HREV, Horiba, France) of wavelength 532 nm was used as the excitation source. To avoid laser heating, the effect of laser power on the samples was tested using different incident radiation powers. Raman shift of the main peak remained unchanged over the laser power between 1 and 10 mW. All reported data were recorded with 5-mW laser power on the samples.

Temperature-dependent Raman measurements between 80 and 705 K were recorded by keeping the sample in a temperature stage (THMS-600, Linkam, UK) equipped with a liquid-nitrogen pump and a temperature controller. Above 450 K ECP cold-water circulator pump was used along with the temperature controller to vary the temperature.

III. RESULTS AND DISCUSSION

The detailed x-ray and neutron-diffraction studies on $Li_{0.5}Fe_{2.5-x}Cr_xO_4$ ($x = 1.1$, 1.3, 1.5, and 1.6) have been reported elsewhere [25,26]. The crystal structure of $Li_{0.5}Fe_{2.5-x}Cr_xO_4$ ($x = 1.1$, 1.3, and 1.5) and $Li_{0.5}Fe_{0.9}Cr_{1.6}O_4$ ($x = 1.6$) belong to $Fd-3m$ and $F-43m$ space groups, respectively. These compounds possess a mixed-spinel structure. There are two crystallographic sites, viz., tetrahedral and octahedral sites, for magnetic (Fe/Cr) cations. Refer to Fig. S1 of Supplemental Material [27]. In the

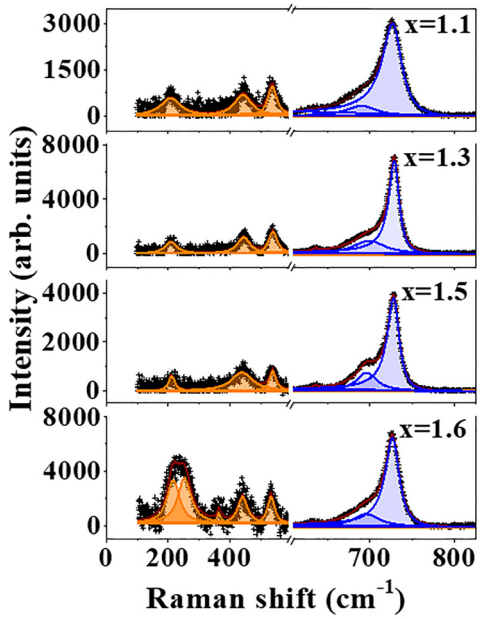

FIG. 1. Raman spectra recorded at 80 K for $Li_{0.5}Fe_{2.5-x}Cr_xO_4$ with $x = 1.1$, 1.3, 1.5, and 1.6. Measured spectra are shown by + symbols. Intensity of the spectral range between 100 and 600 cm^{-1} is multiplied by ×10 for clarity. Deconvoluted components for phonon modes related to octahedral and tetrahedral sites are shown by orange- and purple-shaded areas, respectively. Net fitted spectra are shown by red solid curves. Deconvolution has been carried out considering Fano and Lorentzian functions (will be discussed later).

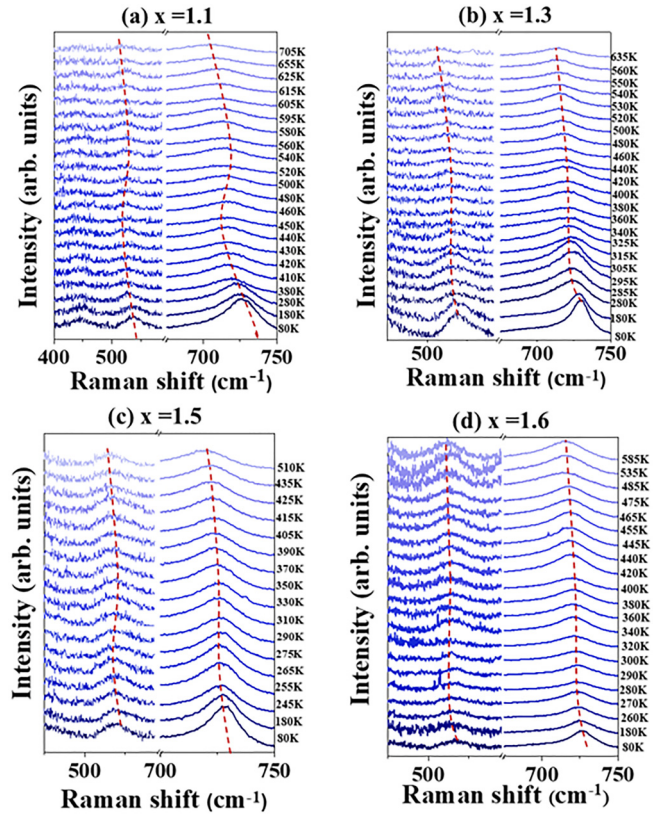

FIG. 2. Characteristic temperature-dependent Raman spectra of $Li_{0.5}Fe_{2.5-x}Cr_xO_4$ for (a) $x = 1.1$, (b) $x = 1.3$, (c) $x = 1.5$, and (d) $x = 1.6$ presenting nonmonotonic shifts in the phonon modes at ∼537 and ∼728 cm^{-1} with temperature (refer to red dashed lines). Set temperature for each spectrum is shown at right in each panel.

unit cell of $Li_{0.5}Fe_{2.5-x}Cr_xO_4$ ($x = 1.1$, 1.3, and 1.5), Fe^{3+}, and Li^+ occupy the tetrahedral site, and $Fe^{3+}/Li^+/Cr^{3+}$ the octahedral site. In contrast, there are two types of tetrahedral sites and one octahedral site for $Li_{0.5}Fe_{0.9}Cr_{1.6}O_4$ ($x = 1.6$). In this unit cell, Fe^{3+} and Li^+ occupy one of the tetrahedral sites, and the other tetrahedral site is occupied by only Fe^{3+} ions. $Fe^{3+}/Li^+/Cr^{3+}$ occupy the octahedral site.

Raman spectra of $Li_{0.5}Fe_{2.5-x}Cr_xO_4$ ($x = 1.1$, 1.3, 1.5, and 1.6) recorded at 80 K over the spectral range between 100 and 800 cm^{-1} are compared in Fig. 1. According to group theory, the irreducible representations of the Raman-active modes at the gamma point for the space group $Fd-3m$ are $\Gamma = A_{1g} + E_g + 3T_{2g}$ ($\Gamma = A_{1g} + E_g + 3T_{2g} + 2T_{1g}$ for the space group $F-43m$). For all compounds, we observe the Raman shifts at around 205, 444, 537, 636, 685, and 728 cm^{-1}. The symmetry and assignment to vibrational modes of these peaks are available in Table S2 of the Supplemental Material [27] following Refs. [28–31]. For $Li_{0.5}Fe_{2.5-x}Cr_xO_4$ ($x = 1.6$), two additional weak peaks at 240 and 360 cm^{-1} are observed. The procedure which we follow to deconvolute the spectra will be discussed later. Deconvoluted spectral components are shown by shaded areas in Fig. 1. In all compounds, the Raman modes below 650 cm^{-1} (deconvoluted components shown by orange-shaded areas in Fig. 1) arise from the octahedral sites, whereas all features above 650 cm^{-1}, shown by purple-shaded areas, originate from the tetrahedral site [28]. Here, we particularly note representative Raman modes at ∼537 (strongest of all peaks from the octahedral lattice site for $x = 1.1$–1.5) and ∼728 cm^{-1}, which correspond to the vibration of Fe–O bonds in the octahedral and tetrahedral sites, respectively. In the rest of this paper, we will refer to these peaks as peak *A* and peak *B*, respectively. It is to be noted that in addition to new peaks, the relative intensities of different modes of the compound with $x = 1.6$ exhibit anomalous behavior, distinctly different from those of $Li_{0.5}Fe_{2.5-x}Cr_xO_4$ ($x = 1.1$, 1.3, and 1.5). A detailed study on this issue will be reported elsewhere.

Characteristic Raman spectra of $Li_{0.5}Fe_{2.5-x}Cr_xO_4$ ($x = 1.1$, 1.3, 1.5, and 1.6), focusing the evolution of two phonon modes *A* and *B*, at 537 and 728 cm^{-1}, with temperature are shown in Fig. 2. The red dashed lines mark the shift in these modes with temperature. As the intensity of the Raman peak at 728 cm^{-1} is much stronger than the lower wave-number spectral features, the intensity scales below and above 600 cm^{-1} are chosen to be different in plotting Fig. 2. All temperature-dependent Raman spectra over the spectral range between 100 and 800 cm^{-1} for all four compounds under study are shown in Figs. S3(a)–S3(d) of the Supplemental Material [27]. The highest temperature for measurements for each compound was chosen depending on the values of their respective T_c. We did not observe the appearance of any new Raman spectral feature between 80 K and the highest temperature of measurements, suggesting there is no structural phase transition in these compounds over the entire temperature range of

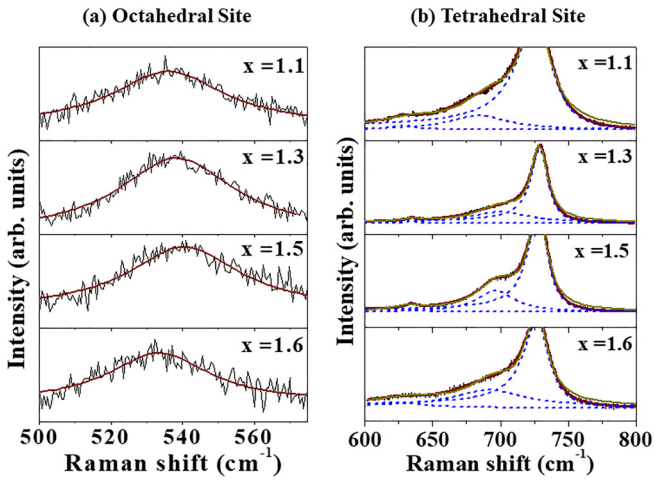

FIG. 3. (a) Raman spectra of $Li_{0.5}Fe_{2.5-x}Cr_xO_4$ for $x = 1.1$, 1.3, 1.5, and 1.6 at 80 K over spectral range between 500 and 575 cm^{-1}. (b) Same over the spectral range between 600 and 800 cm^{-1}. For clarity of line shape towards low wave numbers, intensity axes are not shown in full scale in (b). In (a), red lines are best fit to experimental plots (black) using a Lorentzian function. In (b), best fits to experimental plots (black) obtained with three Lorentzian functions are shown by dark-yellow curves. Red lines are best fits to data points using two Lorentzian functions and a Fano line shape (see text). Deconvoluted components with latter methodology are shown by dashed blue lines.

interest, supporting the earlier findings from neutron-diffraction measurements [26].

The magnified view of peak *A* (black curves) for the compounds at 80 K over the spectral range between 500 and 575 cm^{-1} is shown in Fig. 3(a). All spectra could be fitted with a single Lorentzian function, shown by red solid curves. The magnified view of the spectral range from 600 to 800 cm^{-1} for the compounds is available in Fig. 3(b). Within this spectral range, one expects three Raman modes. Hence, each spectrum was fitted with three Lorentzian functions. The best fits to the data points are shown by dark-yellow solid curves. One notes that there is a clear mismatch between the data points and the fitted curve near the low wave-number tails of the spectra. Such asymmetry of the main peak towards the lower wave number is a signature of the coupling of a phonon with an electron continuum due to Fano resonance. To view this possibility, we fitted the intense peak at 728 cm^{-1} (*B*) with a Fano line shape,

$$I_F(\omega) = F\frac{(q+\varepsilon)^2}{(1+\varepsilon^2)},\ \varepsilon = \frac{(\omega-\omega_0)}{\Gamma}. \quad (1)$$

ω_0 is the spectral peak position, q is the asymmetry parameter, and Γ is the full width at half maximum (FWHM) of peak *B* [32]. *F* is a constant. The other two peaks at 635 and 685 cm^{-1} were fitted with the Lorentzian functions. In this least-square fitting procedure, the peak position, width, and intensity of all peaks, and the Fano asymmetry parameter were allowed to vary freely. The best-fitted curves obtained using this formalism match the measured spectra quite well and are shown by the red curves in Fig. 3(b). The deconvoluted components are shown by blue curves. To exhibit the asymmetry in the line shape of peak *B* and the need for the Fano line shape for analyzing the spectral data points, we do not show the full intensity scale in Fig. 3(b). We refer to Fig. 1 once again. In this figure, the spectra over the spectral range between 100 and 800 cm^{-1} are fitted with a sum of a Fano line shape [in Eq. (1) for peak *B* and five Lorentzian functions for other modes for $Li_{0.5}Fe_{2.5-x}Cr_xO_4$ with $x = 1.1$, 1.3, and 1.5. A Fano line shape and seven Lorentzian functions are used to deconvolute the Raman spectrum of $Li_{0.5}Fe_{2.5-x}Cr_xO_4$ with 1.6 in Fig. 1. Here, we would like to mention that with the increase in Cr^{3+} substitution, both Raman modes *A* and *B* undergo a blueshift till $x = 1.5$. These modes soften for the compound with $x = 1.6$, which is most likely due to the change in the crystal structure.

The variations of Raman shift with temperature for the peaks *A* and *B* of the compounds, as obtained from this analysis, are shown in Figs. 4(a) and 4(b). Panels (i)–(iv) in each set correspond to the data points for $x = 1.1$, 1.3, 1.5, and 1.6, respectively.

A. Spin-phonon coupling

According to Granado *et al.* [33], the shift in phonon frequency ($\Delta\omega$) with temperature in magnetic materials depends on the following factors: (i) lattice expansion, (ii) variation of anharmonic vibrational potential with the temperature at constant volume, (iii) spin-phonon coupling, and (iv) the effect of renormalization of the electronic states on a phonon mode near spin ordering temperature.

The contribution of lattice expansion to the shift in the *j*th phonon mode, $\Delta\omega_j^{\text{latt}}$, can be estimated from the change in lattice volume with temperature. Due to lattice expansion, the phonon frequency shifts by following the relation $\frac{\Delta\omega_j^{\text{latt}}}{\omega} = -\gamma_j\frac{\Delta V}{V}$. ω is the frequency of the *j*th phonon mode, γ_j is Gruneisen's parameter of the same mode, and $\frac{\Delta V}{V}$ is the fractional change in the lattice volume over the temperature. $\frac{\Delta V}{V}$ of these compounds over the temperature range of interest is less than $\sim$0.8% [26], and the mode Gruneisen's parameter of spinel ferrites is $\sim$0.2−0.3 [34–36]. Thus, the observed shift in phonon wave number in Fig. 4 is unlikely due to the lattice expansion with temperature.

With the increase in temperature, the anharmonicity in lattice vibration further modifies the Raman shift ($\Delta\omega_{\text{anh}}$) and FWHM of the phonon modes. If one considers the four-phonon decay scheme in which an optical phonon decays into three acoustic phonon modes, the shift in Raman wave number with temperature follows the relation [37]

$$\omega(T) = \omega_0 + \Delta T$$

$$\Delta(T) = P\left(1+\frac{2}{e^{\frac{\phi}{2}}-1}\right) + Q\left(1+\frac{3}{e^{\frac{\phi}{3}}-1}+\frac{3}{\left(e^{\frac{\phi}{3}}-1\right)^2}\right). \quad (2)$$

Here, $\phi = \hbar\omega_0/k_BT$. *P* and *Q* are anharmonic coefficients, and k_B is the Boltzmann constant. We fit the change in ω with *T* over the entire temperature range using Eq. (2) (refer to Fig S4 of the Supplemental Material [27]). For all four compounds under study, we found anomalous behavior of the data points for both modes *A* and *B* over the temperature range

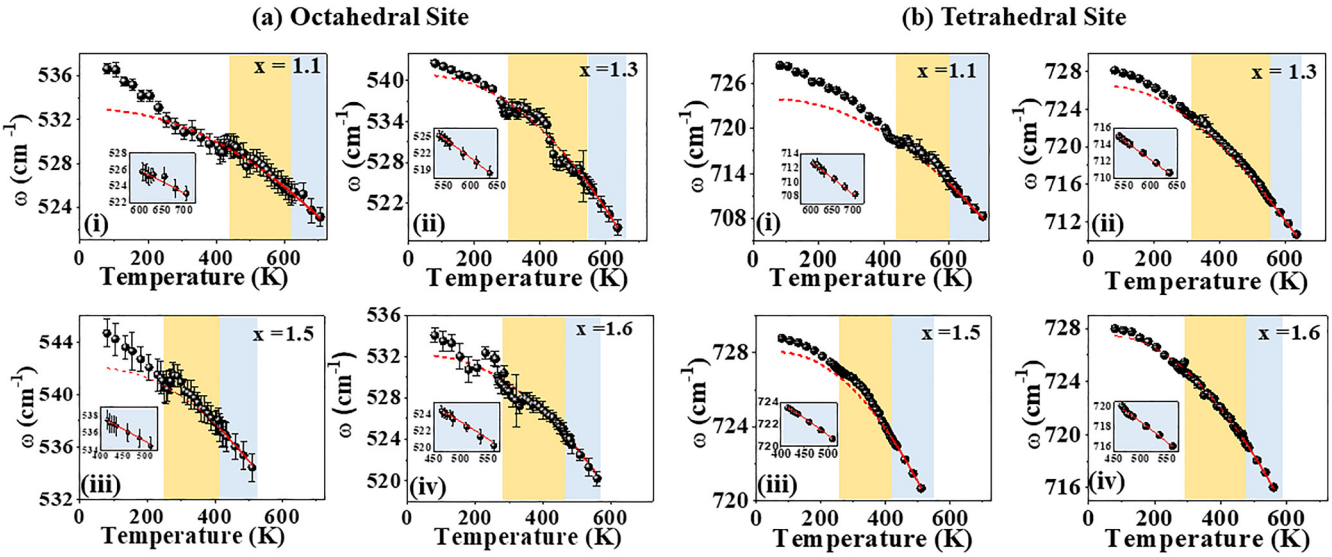

FIG. 4. Variation of Raman shift of peak A and peak B with temperature. Panels (i)–(iv) correspond to the composition with $x = 1.1$, 1.3, 1.5, and 1.6, respectively. In each panel, blue- and yellow-shaded areas mark data points above T_c, and between T_{comp} and T_c, respectively. Red solid line is best fit to data point using Eq. (2) over blue-shaded region (above T_c). Same (data points over T_c and best-fitted curves) is also shown in inset in each panel for clarity. Dashed curves are extrapolation of this best-fitted curve over low-temperature range (below T_c).

between T_{comp} and T_c. The measurements were carried out several times to check the reproducibility of the results.

Above T_c, the compounds are in the paramagnetic phase. Thus, one does not expect any contribution of $\Delta\omega_{sp}$ for $T > T_c$. Thus, we fitted data points of ω vs T plots above T_c (blue-shaded area in Fig. 4) for all compounds using Eq. (2). The best-fitted curves in all panels are shown by solid red lines in Fig. 4. For clarity, the inset in each panel of Fig. 4 presents data points and the fitted curve for the temperature range beyond T_c. The parameters P and Q as obtained for peaks A and B for all compounds are available in Table S5 of the Supplemental Material [27]. These curves are then extrapolated (dashed curves in the panels of Fig. 4) till the lowest value of T. The mismatch between the experimental data points and extrapolated curves indicates that below T_c, apart from anharmonicity, there are other factors that play an important role in the shift of phonon frequency. The shift in phonon mode due to the renormalization of electronic states is usually observed in the case of metals. As the present compounds are insulators, this effect on $\omega-T$ plots can be ignored.

We consider a superexchange spin-spin interaction between two sublattice of the magnetic ions, as suggested from molecular-field theory in Ref. [26]. The coupling between spin and lattice degrees of freedom results in a modulation of J_{ij}. The renormalization of phonon yields a shift in phonon frequency by [38]

$$\Delta\omega_{sp} = \eta\langle \mathbf{S}_i.\mathbf{S}_j\rangle. \tag{3}$$

η, which depends on second-order partial derivative of superexchange interaction with respect to the normal coordinate of the phonon mode, determines the phonon-spin coupling strength. $\langle S_i.S_j\rangle$ is the scalar spin-spin correlation function between the ith and the jth magnetic ions in two sublattices. One further considers

$$\langle \mathbf{S}_i.\mathbf{S}_j\rangle = f\left|\frac{M(T)}{M(S)}\right|^2, \tag{4}$$

where $M(S)$ and $M(T)$ are magnitudes of saturation magnetization and the magnetization of the crystal per ion at a given temperature. The factor f takes care of the number of sublattices of magnetic sites in the system ($f = 2$ for $x = 1.1$, 1.3, and 1.5; $f = 3$ for $x = 1.6$).

As mentioned earlier, below the magnetic-ordering temperature T_c, $Li_{0.5}Fe_{2.5-x}Cr_xO_4$ ($x = 1.1$, 1.3, and 1.5) exhibit magnetic compensation at T_{comp} and a relatively high magnetization at T_m for $T_{\text{comp}} < T_m < T_c$ (refer to Table I). Below T_{comp} the magnetization monotonously increases with the decrease in temperature. The temperature-dependent neutron-diffraction studies [25,26] revealed that the magnetic moments in octahedral and tetrahedral crystallographic sites are aligned antiparallel to each other. The resultant magnetic moment could be estimated [25,26] from the relation $|M\text{net}| = 2|MO| - |MT|$, where MT and MO are the magnetic moments in the tetrahedral and octahedral sites, respectively. At T_{comp} the resultant magnetization goes to zero. Following Eqs. (3) and (4), to study the correlation between $\Delta\omega$ and spin ordering in this system, Fig. 5(a) plots $|M(T)/M(S)|^2$ with temperature for $Li_{0.5}Fe_{2.5-x}Cr_xO_4$ ($x = 1.1$, 1.3, 1.5, and 1.6) as obtained from Ref. [25]. Insets show the magnified view of the plots between T_{comp} and T_c. We estimate the electronic contribution to Raman shift ($\Delta\omega$) by taking the difference between experimental data points and the fitted/extrapolated curve from Fig. 4 for peaks A and B in the octahedral and the tetrahedral sites. Figures 5(b) and 5(c) plot $\Delta\omega$ vs $|M(T)/M(S)|^2$ for peak A (in the octahedral site) and peak B (in the tetrahedral site) for all compounds, respectively. The color of each data point in Figs. 5(a)–5(c) follows the temperature scale shown below the plots. Note T_{comp}, T_m, and T_c in the color bar. It is interesting to note

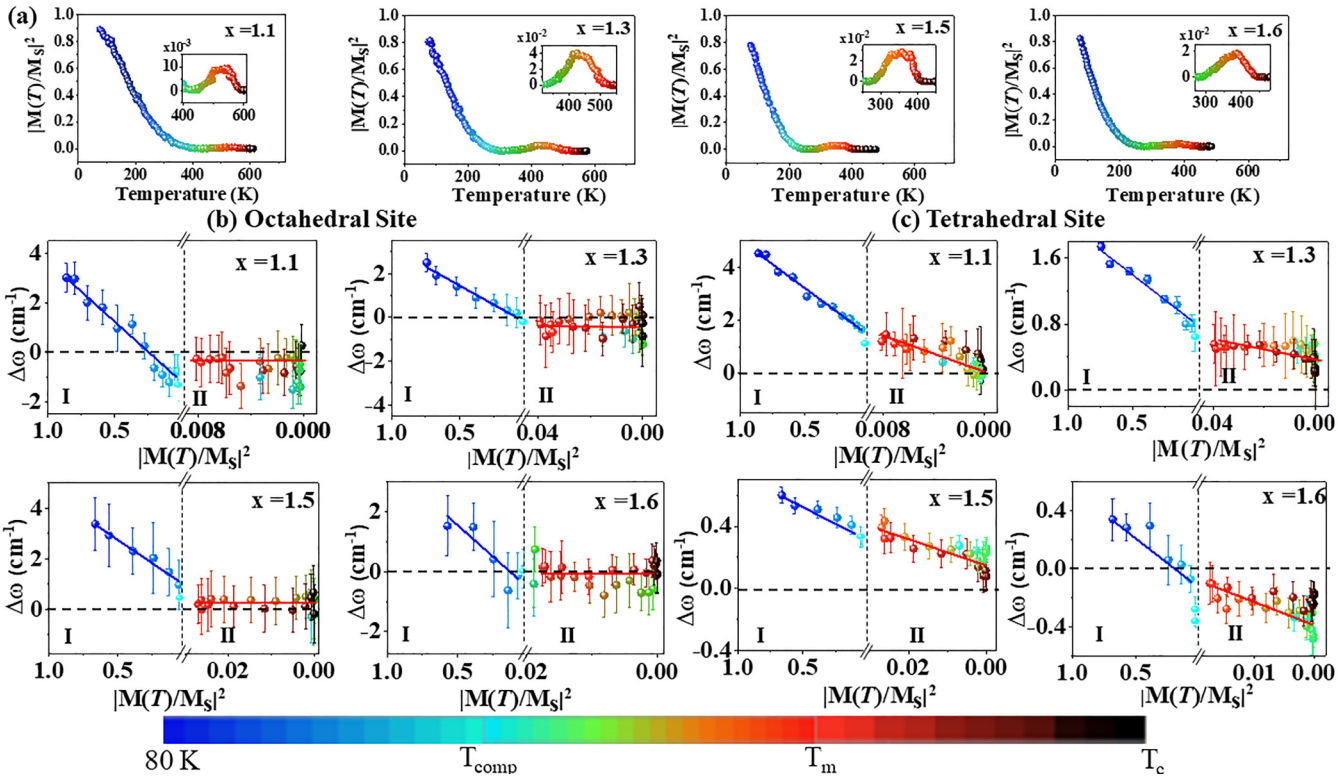

FIG. 5. (a) Variation of $|M(T)/M(S)|^2$ with temperature for $Li_{0.5}Fe_{2.5-x}Cr_xO_4$ ($x = 1.1$, 1.3, 1.5, and 1.6). Insets show the magnified view between T_{comp} and T_c for all compounds. $\Delta\omega$ vs $|M(T)/M(S)|^2$ plots are shown in (b) for peak A in octahedral site and (c) for peak B in tetrahedral site. Color map of symbols in all plots [(a)–(c)] follows temperature scale presented at bottom. Vertical dashed lines in (b) and (c) mark two regions, region I (below T_{comp}) and region II (between T_c and T_{comp}). Note T_{comp}, T_m, and T_c in color scale. Regions I and II in (b) and (c) correspond to regime of two different slopes (spin-phonon coupling strengths). Best linear fit to data points in these two regions in (b) and (c) are shown by blue and red solid lines, respectively. Horizontal dashed lines mark zero scale of $\Delta\omega$.

that all plots in Figs. 5(b) and 5(c) are bilinear. We split the full range of $\Delta\omega$ vs $|M(T)/M(S)|^2$ plots into two regions I and II, separated by dashed lines in Fig. 5. Data points in region I correlate with temperature $T \ll T_{comp}$. Region II in all panels corresponds to the temperature range just below $T_{comp}(T < T_{comp})$ to T_c. A careful scrutiny of the color map of the symbols reveals that the data points in all panels of Figs. 5(b) and 5(c) enter in region II (from region I on the left side) just below T_{comp} (minimum value of $|M(T)/M(S)|^2$), move up towards higher values of $|M(T)/M(S)|^2$ (from right to left) and then turn from left to right following the trend in magnetization vs temperature plot in Fig. 5(a). We have excluded the data points representing the paramagnetic phase [$M(T) \approx 0$ and $\Delta\omega \approx 0$] to focus on the spin-phonon coupling in the magnetically ordered phase of the compounds. Using Eqs. (3) and (4), we estimate the spin-phonon coupling coefficients $\eta 1$ (obtained from the slope of the linear fit to data points in region I), and $\eta 2$ (from the slope of the linear fit to all data points in region II). The values of $\eta 1$ and $\eta 2$ for peak A in the octahedral site and B in the tetrahedral site of all compounds are listed in Table II.

We infer the following: Magnetoelastic couplings in two magnetic sublattice sites between T_{comp} and T_c are appreciably different. While the spin-phonon coupling strength is higher in region II ($T_{comp} < T < T_c$) for all compounds than in region I ($T_{comp} \gg T$) in the tetrahedral sublattice site, and the same is nearly negligible (within the error bar) above T_{comp} for the octahedral site. The above observation suggests a strong magnetoelastic coupling at the tetrahedral site. A weaker magnetoelastic coupling at the octahedral site may result from the spin disorder due to the presence of both Fe and Cr ions at this site. On the other hand, the tetrahedral site, having only Fe spins, is strongly coupled to the lattice [25]. The mean-field theory suggests that the magnetic moments in the tetrahedral sites dominate over the octahedral site of these compounds [25]. Furthermore, the systematic drop in η_1 and η_2 of the tetrahedral site and η_1 of the octahedral site for $x = 1.1$-1.5, respectively, is possibly due to the increase in substitutional disorder in the compound (refer to Fig. S6 of the Supplemental Material [27]).

$|M(T)/M(S)|^2$ in Fig. 5 corresponds to the net magnetization involving both magnetic sublattices. The observed one-to-one correlation between $|M(T)/M(S)|^2$ and $\Delta\omega$ of each sublattice may arise due to cross correlation between two sublattices. In Fig. 5, the role of phonon in determining magnetic compensation phenomenon is reflected as there is a clear change in the slope of $\Delta\omega$ vs $|M(T)/M(S)|^2$ plot at just below T_{comp}. Moreover, there is a systematic drop in T_{comp} with composition from $x = 1.1$ to $x = 1.5$ of the system (refer to Table I), while the spin-phonon coupling strength decreases accordingly. In other words, for weaker spin-phonon coupling, the magnetic compensation could be achieved only at a lower temperature. The slight difference in the trend in the values of η_1 and η_2 for the compound $x = 1.6$ is most probably

TABLE II. Spin-phonon coupling constants η_1 and η_2 as obtained from analysis of peaks A and B in octahedral and tetrahedral sites, respectively, as obtained from Fig. 5. Highest value of $|1/q|$ and corresponding temperature (between T_{comp} and T_c, as obtained from Fig. 6).

	Octahedral site (peak A)		Tetrahedral site (peak B)		Tetrahedral site (peak B)
x	η_1	η_2	η_1	η_2	$\|1/q\|_{max}$ @ T
1.1	2.7 ± 0.3	1.3 ± 36	1.8 ± 0.1	36 ± 12	0.14 ± 0.07 @ 510K
1.3	2.0 ± 0.2	0.4 ± 6	0.6 ± 0.1	6.0 ± 1	0.13 ± 0.02 @ 370K
1.5	1.9 ± 0.2	0.1 ± 9	0.19 ± 0.02	2.8 ± 0.7	0.097 ± 0.004 @ 265K
1.6	1.3 ± 0.4	0.2 ± 4	0.23 ± 0.03	2.0 ± 1	0.160 ± 0.006 @ 320K

due to the change in the crystal structure. It is to be noted that η is related to the superexchange integral J between magnetic ions [38]. A lower value of η possibly results in a lower value of J_{ij} in the compound $x = 1.5$ than in $x = 1.1$, and hence the value of T_{comp} for $x = 1.5$ is less than that for the $x = 1.1$ compound.

The spin-phonon coupling in these compounds is further validated by the analysis of spectral line shape. It is to be recalled that the above-discussed most intense Raman peak B (at $\sim$728 cm^{-1}) in the tetrahedral site could be best fitted with a Fano line shape. As mentioned earlier, such line shape arises due to the coupling of phonon mode with a continuum of electronic excitations in a similar energy range. The inverse of the Fano asymmetric parameter, $|1/q|$, carries the information of electron-phonon coupling strength either due to charge ordering or spin alignment [24]. While the coupling of phonon with electronic density contributes to Raman linewidth and negligibly to Raman shift, it is the other way when the same phonon mode couples with the spin of the electron. For $|q| \gg 1$ and $|q| \ll 1$, the phononic and electronic contributions, respectively, dominate. $|q| = 1$ corresponds to a comparable contribution of both.

The variation of $|1/q|$ with temperature for all compounds, as obtained from the curve-fitting procedure, is shown in Fig. 6. We observe a decrease in coupling strength with the increase in temperature along with its anomalous behavior between T_{comp} and T_c (shown by shaded areas). The values of $|q|$ over the entire temperature range of all compounds are much higher than 1, suggesting a strong contribution of phonons in spin-phonon coupling in these systems. Moreover, the maximum value of $|1/q|_{max}$ varies in the same fashion as η_2 of the tetrahedral site, obtained from the analysis of the same phonon mode (see Table II). It drops for the compounds with $x = 1.1$ to $x = 1.5$, and then slightly increases for $x = 1.6$. Thus, Figs. 5 and 6 reveal strong interlinkage of spin and lattice degrees of freedom in $Li_{0.5}Fe_{2.5-x}Cr_xO_4$ ($x = 1.1$, 1.3, 1.5, and 1.6) coupling at the tetrahedral site between T_{comp} and T_c. Here, we would like to mention that in Fig. 6 $|1/q|_{max}$ appears at 510, 370, 265 (30, 70, and 85 K below T_m) for compounds with $x = 1.1$, 1.3, and 1.5, respectively. In the case of the compound with $x = 1.6$, the $|1/q|_{max}$ is attained 70 K below T_m. Since Fano resonance results from the coupling of discrete phonon states with electron continuum, the observed (i) drop in $|1/q|_{max}$ and (ii) onset of the downturn of the asymmetric Fano parameter beyond its maximum value at a systematically much lower temperature than T_m with the increase in x are most likely due to the increase in disorder with Cr substitution in these compounds when the coupling between the spin and lattice degrees of freedom starts to break down at a lower temperature. It is to be recalled that the value of T_c also decreases with x. A slightly different behavior of $|1/q|_{max}$ in the compound with $x = 1.6$ is possibly due to its different crystal structure.

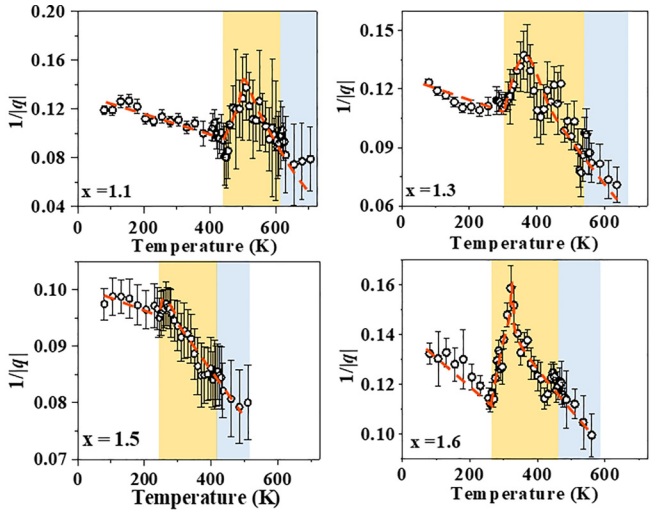

FIG. 6. Variation of $|1/q|$ with temperature for different compositions of $Li_{0.5}Fe_{2.5-x}Cr_xO_4$ ($x = 1.1$, 1.3, 1.5, and 1.6). Orange dashed curves are guides to the eyes. In all panels, regions between T_{comp} and T_c/above T_c are marked by yellow-/blue-shaded areas.

B. Coupling of phonon and electronic density of states

Next, we look into the variation of spectral width (FWHM) for peak B with temperature for all compounds, as shown in Fig. 7(a). Due to the increase in anharmonicity, the FWHM increases with the increase in temperature by following the relation [37]

$$\Gamma(T) = C\left(1 + \frac{2}{e^{\phi/2} - 1}\right) + D\left(1 + \frac{3}{e^{\phi/3} - 1} + \frac{3}{(e^{\phi/3} - 1)^2}\right). \quad (5)$$

C and D are anharmonicity coefficients. Unlike the variation of Raman shift with temperature in Fig. 4, for all four compounds, data points in all panels in Fig. 7(a) could be best matched with Eq. (5) for values of C and D (see Table S5 in the Supplemental Material [27]).

The real and imaginary parts of the self-energy of the phonon due to electron-phonon interaction govern the changes in Raman wave number and FWHM. It is possible that change

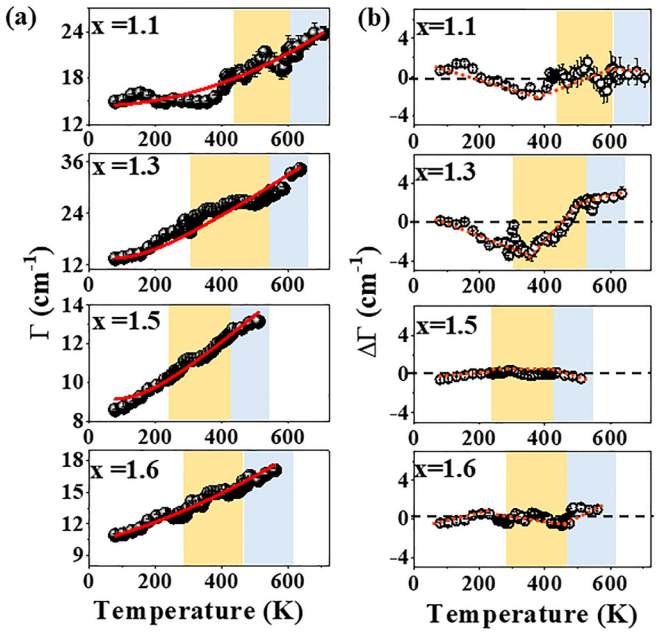

FIG. 7. (a) Variation of Raman linewidth with temperature for the B in $Li_{0.5}Fe_{2.5-x}Cr_xO_4$ ($x = 1.1$, 1.3, 1.5, and 1.6). Red solid lines are best fits to data points using Eq. (5). (b) Variation of $\Delta\Gamma$ with temperature for all compounds. Orange dashed lines are guides to the eyes. Region between T_{comp} and T_c/above T_c are marked by yellow-/blue-shaded areas for compounds. Black dashed lines mark zero value of $\Delta\Gamma$.

in the imaginary component is less affected by the interaction and hence, does not affect the FWHM of peak B considerably, unlike its peak position [24]. Nonetheless, if we subtract the data points from the best-matched line, representing the anharmonic contribution to phonon self-energy in Fig. 7(a), we find an interesting trend; see Fig. 7(b) (orange lines are guides to the eyes).

Due to electron-phonon coupling, the nonequilibrium electron distribution at a certain temperature returns to local equilibrium via the distribution of energy between electronic and lattice subsystems [39,40]. This affects the phonon linewidth and reflects the contribution of electron density in electron-phonon coupling in the system. The electron-phonon coupling renormalization for a particular phonon mode can be calculated from Allen's formulation [39,41–43]:

$$\lambda = \frac{g_i}{2\pi N(E_F)} \frac{\Gamma_i}{\omega_b^2} \tag{6}$$

Here, g_i is the degeneracy of the corresponding phonon mode, $N(E_F)$ is the density of states per each spin per unit cell at the Fermi level, Γ_i is the FWHM of the particular phonon mode, and ω_b is the bare frequency (frequency without any coupling). Thus, the variation of $\Delta\Gamma$ with temperature, as shown in Fig. 7(b), reflects the alteration of the FWHM due to the coupling of electron density of states at the Fermi level and the phonon mode. We note that there is a change in slope just below T_{comp} and at T_c. The values of $\Delta\Gamma$ are relatively high for the compounds $x = 1.1$ and $x = 1.3$, and nearly zero for $x = 1.5$ and $x = 1.6$. The reduction in the coupling of electron and lattice degrees of freedom in $x = 1.5$ and 1.6 may be due to the substitutional disorder with the increase in doping concentration.

dc and ac conductivity measurements on the same samples are reported elsewhere [25]. In this paper [25], the frequency-dependent ac conductivity plots at various temperatures are fitted with the equation $\sigma_{ac} = \sigma_{dc} + \alpha\omega^n$, where α and n are constants. The parameter n relates to the translational motion of the ions in $Li_{0.5}Fe_{2.5-x}Cr_xO_4$. The variation of n with temperature is available in Fig. S7 of the Supplemental Material [27]. For all compounds, the slope of the n vs T plot changes at T_{comp} and T_c. Such behavior of the n vs T plot has been attributed to a strong coupling between the magnetic and electric degrees of freedom in this system. In Fig. 7(b), when we compare $\Delta\Gamma$ vs T plot, we find a very similar trend. Like n, not only the slopes of $\Delta\Gamma$ vs T change at T_{comp} and T_c, but also the value of $\Delta\Gamma$ drops for the compounds with $x = 1.1$ to $x = 1.6$. As discussed above, $\Delta\Gamma$ is related to the electronic density of states. Thus, such behavior of $\Delta\Gamma$ vs T plots most likely indicates a strong coupling of the same phonon mode, which exhibits magnetoelastic coupling, with the electrical degrees of freedom and plays a crucial role in determining the electrical conductivity of the system. Because of the very weak intensity, the standard deviation (as obtained from the fitting procedure) of FWHM of peak A was too high to draw any meaningful conclusion on its evolution with temperature.

IV. SUMMARY

In this paper, we have shown the role of phonon in cross talk between two magnetic sublattices in $Li_{0.5}Fe_{2.5-x}Cr_xO_4$. The exotic magnetic behavior in this system arises due to magnetic ions in both tetrahedral and octahedral sites. Temperature-dependent micro-Raman spectroscopic measurements reveal anomalous behavior of Raman shift with temperature below the magnetic-ordering temperature. The bilinear plot of the variation of electronic contribution to phonon frequency ($\Delta\omega$) and square of relative magnetization $|M(T)/M(S)|^2$ suggests spin-lattice interaction strengths of two different magnitudes are present in these compounds over the temperature range under study. Between just below T_{comp} and T_c, while the magnetoelastic coupling in the tetrahedral site becomes stronger, the same nearly vanishes in the octahedral site. Furthermore, a direct correlation between $|M(T)/M(S)|^2$ and $\Delta\omega$ across magnetic compensation further indicates the role of phonon in governing this magnetic phenomenon. The Fano line shape of the oxygen vibration of the Fe–O bond in the tetrahedral site and the anomalous behavior of Fano asymmetry parameters between T_{comp} and T_c further confirm an interlinkage between spin and lattice degrees of freedom in these compounds. The anomaly in the variation of Raman linewidth with temperature is exploited to determine electron-phonon coupling in $Li_{0.5}Fe_{2.5-x}Cr_xO_4$. Our results suggest that a crucial role is played by phonon dynamics in governing the interplay between spin and electrical degrees of freedom in these compounds. Further, the magnetic compensation phenomenon deals with net null magnetization (involving a fascinating interplay of the temperature dependence of site moments of more than one magnetic sublattice). Hence, it can be used in the spin-resolving devices

without any hindrance from a stray magnetic field from the magnet [44]. The present study is also significant in the area of battery materials as it deals with the phonon dynamics involving Li ions coupled with interesting electronic and magnetic behaviors.

ACKNOWLEDGMENTS

A.R. and S.M.Y. acknowledge the Board of Research in Nuclear Sciences in India (Grant No. 58/14/24/2019-BRNS) for the financial assistance. A.R. thanks Sudhansu Sekhar Mandal, IIT Kharagpur, for the valuable discussion.

[1] F. Pomiro, R. D. Sánchez, G. Cuello, A. Maignan, C. Martin, and R. E. Carbonio, Spin reorientation, magnetization reversal, and negative thermal expansion observed in $RFe_{0.5}Cr_{0.5}O_3$ perovskites (R = Lu,Yb,Tm), Phys. Rev. B **94**, 134402 (2016).

[2] Deepak, A. Kumar, S. M. Yusuf, and E. V. Sampathkumaran, Insight into the negative magnetization and anomalous exchange-bias in $DyFe_5Al_7$ through neutron depolarization and neutron diffraction studies, J. Phys. Condens Matter. **35**, 065802 (2023).

[3] R. Vilarinho, M. C. Weber, M. Guennou, A. C. Miranda, C. Dias, P. Tavares, J. Kreise, A. Almeida, and J. A. Moreira, Magnetostructural coupling in $RFeO_3$ (R = Nd, Tb, Eu, and Gd), Sci. Rep. **12**, 9697 (2022).

[4] D. Amoroso, Bertrand Dupé, and M. J. Verstraete, Unraveling the role of Sm 4f electrons in the magnetism of $SmFeO_3$, Phys. Rev. B **107**, 104427 (2023).

[5] I. Fita, A. Wisniewski, R. Puzniak, V. Markovich, and G. Gorodetsky, Exchange-bias reversal in magnetically compensated $ErFeO_3$ single crystal, Phys. Rev. B **93**, 184432 (2016).

[6] P. Gupta and D. Pal, Spin induced exchange bias and lattice modulation in $Nd_{1-x}Eu_xCrO_3$, J. Phys. Condens. Matter. **33**, 135806 (2021).

[7] C. Li, Y. Qiu, G. O. Barasa, and S. Yuan, Spin reorientation, normal and inverse magnetocaloric effects in heavy rare-earth iron garnets, Ceram Int. **46**, 18758 (2020).

[8] R. Zhao, C. Yang, H. Wang, K. Jiang, H. Wu, S. Shen, L. Wang, Y. Sun, K. Jin, J. Gao, L. Chen, H. Wang, J. L. M. Driscoll, P. A. v. Aken, J. Hong, W. Li, and H. Yang, Emergent multiferroism with magnetodielectric coupling in $EuTiO_3$ created by a negative pressure control of strong spin-phonon coupling, Nat. Commun. **13**, 2364 (2022).

[9] R. Ramesh and D. G. Schlom, Creating emergent phenomena in oxide superlattices, Nat. Rev. Mater., **4**, 257 (2019).

[10] W. Lafargue-Dit-Hauret, D. Braithwaite, A. D. Huxley, T. Kimura, A. Saúl, and X. Rocquefelte, Potential room-temperature multiferroicity in cupric oxide under high pressure, Phys. Rev. B **103**, 214432 (2021).

[11] M. Basini, M. Martina, B. Pancaldi, B. Wehinger, M. Udina, T. Tadano, M. C. Hoffmann, A. V. Balatsky, and S. Bonetti, Terahertz electric-field driven dynamical multiferroicity in $SrTiO_3$, arXiv:2210.01690.

[12] I. Ardizzone, J. Teyssier, I. Crassee, A. B. Kuzmenko, D. G. Mazzone, D. J. Gawryluk, M. Medarde, and D. van der Marel, Raman spectroscopic evidence for multiferroicity in rare earth nickelate single crystals, Phys. Rev. Res. **3**, 033007 (2021).

[13] Z. Liu, Y. Araki, T.-h. Arima, S. Itoh, S. Asai, and T. Masuda, Spin excitation in the coupled honeycomb lattice compound Ni_2InSbO_6, Phys. Rev. B **107**, 064428 (2023).

[14] N. Leo, V. Carolus, J. S. White, M. Kenzelmann, M. Hudl, P. Tolédano, T. Honda, T. Kimura, S. A. Ivanov, M. Weil, T. Lottermoser, D. Meier, and M. Fiebig, Magnetoelectric inversion of domain patterns, Nature (London) **560**, 466 (2018).

[15] J. K. H. Fischer, H. Ueda, and T. Kimura, Domain switching and exchange bias control by electric field in the multiferroic conical magnet Mn_2GeO_4, Phys. Rev. B **102**, 054412 (2020).

[16] M. C. Weber, M. Guennou, D. M. Evans, C. Toulouse, A. Simonov, Y. Kholina, X. Ma, W. Ren, S. Cao, M. A. Carpenter, B. Dkhil, M. Fiebig, and J. Kreisel, Emerging spin–phonon coupling through cross-talk of two magnetic sublattices, Nat. Commun. **13**, 443 (2022).

[17] S. Artyukhin, M. Mostovoy, N. P. Jensen, D. Le, K. Prokes, V. G de Paula, H. N Bordallo, A. Maljuk, S. Landsgesell, H. Ryll, B. Klemke, S. Paeckel, K. Kiefer, K. Lefmann, L. T. Kuhn, and D. N Argyriou, Solitonic lattice and Yukawa forces in the rare earth orthoferrite $TbFeO_3$, Nat. Mater. **11**, 694 (2012).

[18] J. M. Lai, Y. R. Xie, and J. Zhang, Detection of electron–phonon coupling in two-dimensional materials by light scattering, Nano Res **14**, 1711 (2021).

[19] M. Opačić, N. Lazarević, M. M. Radonjić, M. Šćepanović, H. Ryu, A. Wang, D. Tanasković, C. Petrovic, and Z. V. Popović, Raman spectroscopy of $K_xCo_{2-y}Se_2$ single crystals near the ferromagnet–paramagnet transition, J. Phys. Condens Matter. **28**, 485401 (2016).

[20] D. Chen, Y. L. Jia, T. T. Zhang, Z. Fang, K. Jin, P.Richard, and H. Ding, Raman study of electron-phonon coupling in thin films of the spinel oxide superconductor $LiTi_2O_4$, Phys. Rev. B **96**, 094501 (2017).

[21] A. Sunny, A. Thirumurugan, and K. Balasubramanian, Laser induced Fano scattering, electron–phonon coupling, bond length and phonon lifetime changes in α-Fe_2O_3 nanostructures, Phys. Chem. Chem. Phys. **22**, 2001 (2020).

[22] M. Gupta, A. Kumar, A. Sagdeo, and P. R. Sagdeo, Doping-induced combined Fano and phonon confinement effect in La-Doped CeO_2: Raman spectroscopy analysis, J. Phys. Chem. C **125**, 2648 (2021).

[23] A. Kumar, S. Chaudhary, D. K. Pandya, and S. K. Sharma, Evidence of electron-phonon and spin-phonon couplings at the Verwey transition in Fe_3O_4, Phys. Rev. B **90**, 024302 (2014).

[24] A. Thomas, P. Telang, K. Mishra, M. Cesnek, J. Bednarcik, D. V. S. Muthu, S. Singh, and A. K. Sood, Role of spin-phonon and electron-phonon interactions in the phonon renormalization of $(Eu_{1-x}Bi_x)_2Ir_2O_7$ across the metal-insulator phase transition: Temperature-dependent Raman and x-ray studies, Phys. Rev. B **105**, 075145 (2022).

[25] M. Ghanathe, A. K. Bera, A. Kumar, and S. M. Yusuf, Mixed ionic−electronic conduction and magnetoelectric coupling in $Li_{0.5}Fe_{2.5-x}Cr_xO_4$ (x = 1.0, 1.1, 1.3, 1.5, and 1.6) involving magnetization compensation phenomenon, ACS Appl. Electronic. Mater. **4**, 394 (2022).

[26] M. Ghanathe, A. Kumar, and S. M. Yusuf, Microscopic and mesoscopic understanding of magnetization compensation phenomenon in ferrimagnetic $Li_{0.5}FeCr_{1.5}O_4$ spinel, J. Appl. Phys. **125**, 093903 (2019).

[27] See Supplemental Material at http://link.aps.org/supplemental/10.1103/PhysRevB.108.014438. S1: Crystal structure of $Li_{0.5}Fe_{2.5-x}Cr_xO_4$. S2: Observed Raman modes at 80 K in $Li_{0.5}Fe_{2.5-x}Cr_xO_4$ and their assignments. S3: Evolution of Raman spectra of $Li_{0.5}Fe_{2.5-x}Cr_xO_4$ with temperature. S4: Evolution of Raman shifts with temperature and the fitted curves. S5: Coefficients of anharmonicity for the Raman modes. S6: Variation of spin-phonon coupling constants with relative Cr occupancies. S7: Evolution of frequency exponent n of ac conductivity with temperature. It also contains Refs. [28–31].

[28] K. Sabei, A. Rais, K. Taibi, M. Moreau, B. Ouddane, and A. Addou, Structural Rietveld refinement and vibrational study of $MgCr_xFe_{2-x}O_4$, Phys. B: Condens. Matter **501**, 38 (2016).

[29] N. Bouhadouza, A. Rais, S. Kaoua, M. Moreau, K. Taibi, and A. Addou, Structural and vibrational studies of $NiAl_xFe_{2-x}O_4$ ferrites ($0 \leqslant x \leqslant 1$), Ceram. Int. **41**, 11687 (2015).

[30] D. Varshney and K. Verma, Substitutional effects on structural and dielectric properties of $Ni_{1-x}A_xFe_2O_4$ (A = Mg, Zn), Mater. Chem. Phys **140**, 412 (2013).

[31] V. D'Ippolito, G. B. Andreozzi, D. Bersanib, and P. P. Lotticib, Raman fingerprint of chromate, aluminate and ferrite spinels, J. Raman Spectrosc. **46**, 1255 (2015).

[32] U. Fano, Effects of configuration interaction on intensities and phase shifts, Phys. Rev. **124**, 1866 (1961).

[33] E. Granado, A. Garcıa, J. A. Sanjurjo, C. Rettori, I. Torriani, F. Prado, R. D. Sanchez, A. Caneiro, and S. B. Oseroff, Magnetic ordering effects in the Raman spectra of $La_{1-x}Mn_{1-x}O_3$, Phys. Rev. B **60**, 11879 (1999).

[34] Z. W. Wang and S. K. Saxena, Pressure induced phase transformations in nanocrystalline maghemite (γ-Fe_2O_3), Solid State Commun. **123**, 195 (2002).

[35] O. N. Shebanova and P. Lazor, Vibrational modeling of the thermodynamic properties of magnetite Fe_3O_4 at high pressure from Raman spectroscopic study, J. Chem. Phys. **119**, 6100 (2003).

[36] S. Rahman, S. Samanta, D. Errandonea, S. Yan, K. Yang, J. Lu, and L. Wang, Pressure-induced structural evaluation and insulator-metal transition in the mixed spinel ferrite $Zn_{0.2}Mg_{0.8}F_2O_4$, Phys. Rev. B **95**, 024107 (2017).

[37] M. Balkanski, R. F. Wallis, and E. Haro, Anharmonic effects in light scattering due to optical phonons in silicon, Phys. Rev. B **28**, 1928 (1983).

[38] W. Baltensperger, Influence of magnetic order on conduction electrons and phonons in magnetic semiconductors, J. Appl. Phys. **41**, 1052 (1970).

[39] P. B. Allen, Theory of Thermal Relaxation of Electrons in Metals, Phys. Rev. Lett. **59**, 1460 (1987).

[40] S. Sadasivam, M. K. Y. Chan, and P. Darancet, Theory of Thermal Relaxation of Electrons in Semiconductors, Phys. Rev. Lett. **119**, 136602 (2017).

[41] P. B. Allen, Effect of soft phonons on superconductivity, Solid State Commun. **14**, 937 (1974).

[42] S. Bhattacharjee and K. K. Chattopadhyay, Laser-induced Fano asymmetry, electron-phonon coupling, and phase transition in lanthanide sesquioxide (Ln_2O_3; Ln = Eu, Gd, Dy) nanoparticles: A Raman spectroscopic investigation, J. Appl. Phys. **132**, 215107 (2022).

[43] Y. Zhang, L. Yan, W. Wu, G. He, J. Zhang, Z. Ni, X. Jiang, M. Qin, F. Jin, J. Yuan, B. Zhu, Q. Chen, L. Zhou, Y. Li, J. Luo, and K. Jin, Single-crystalline transition metal phosphide superconductor WP studied by Raman spectroscopy and first-principles calculations, Phys. Rev. B **105**, 174511 (2022).

[44] A. Kumar and S. M. Yusuf, The phenomenon of negative magnetization and its implications, Phys. Rep. **556**, 1 (2015).